Towards prediction of wind load on pylons for a neutral atmospheric boundary layer flow over two successive hills

Karim Adib, Adrien Thacker, Dominique Astruc, Frédéric Yann Moulin

Towards prediction of wind load on pylons for a neutral atmospheric boundary layer flow over two successive hills

Adib Karim[a], Thacker Adrien[a], Astruc Dominique[a], Moulin Y. Frédéric[a]

[a] *Institut de Mécanique des Fluides de Toulouse, IMFT, Université de Toulouse, CNRS - Toulouse, FRANCE*

Abstract

In strong wind situations for a neutral atmospheric boundary layers, wind loads on pylons depend on both the mean velocity and the turbulence fluctuations, predicted by analytical models only for simple topographies. For complex topographies, only experiments or numerical simulations give access to the local flow conditions around the pylon. We present experimental and numerical results using a RANS model for the parametric study of the flow near two successive hills of height H and width L for varying distance λ between the tops. We focus on the modification of flow conditions on the second hill by the presence of the first hill. For $\lambda/H \geq 19.2$, the first hill does not modify the flow structure around the second hill. For decreasing values of λ/H below 19.2, a secondary turbulence intensity peak appears on the frontal part of the second hill. It is associated with the impact of the mixing layer generated at the top of the first hill, whose development is well described by analytical models of the planar mixing layer. These analytical models yields simple estimations of the turbulent kinetic energy k for the pylon's wind load calculations. Different hill slopes and height ratios are also investigated.

Keywords: 2D hill, flow over hill, successive hills, mixing layer model, atmospheric boundary layer, turbulent boundary layer, k-ϵ

1. Introduction

For pylon design, calculations take into account the load on the pylon. The wind load is a major contribution to the total load, in particular during strong wind atmospheric events, and yet, the hardest to predict and describe when flow occurs over complex topographies.

In strong wind situations, neutral atmospheric boundary layer conditions are generally observed. For such flows over shallow topographies, Jackson and Hunt (1975) proposed an analytical model to predict the mean flow perturbation of an upstream log-law velocity profile. Hunt et al. (1988) then improved this model and compared successfully their predictions with field measurements (Mason and Sykes (1979); Mason and King (1985); Taylor and Teunissen (1987)) and wind tunnel measurements (Gong and Ibbetson (1989); Finnigan et al. (1990)) for flows over hills. Shallow hills are generally defined as hills with slope S below 0.2, where S is the ratio between the hill's height H and its width L (taken at mid-height). It is related to the observation made by Finnigan (1988) on a collection of field and wind tunnel data that flow separation downstream of the hill occurs for hills with $S > 0.3$ (so called steep hill) whereas no separation is detected for hills with $S < 0.2$. The success of the analytical model of Hunt et al. (1988) for shallow topographies motivated its integration into Eurocode formulae for the prediction of topographic effects on local wind velocity amplification.

For steep hills, the analytical model of Hunt et al. (1988) is generally applied with caution, and for the upstream face only. This approach is validated by several studies that have been conducted for flows around two dimensional isolated rough hills using Reynolds-averaged Navier-Stokes (RANS) equations with a k-epsilon turbulence model (Castro and Apsley (1997), Griffiths and Middleton (2010) and Safaei Pirooz and Flay (2018)) or a Reynolds stress model (Loureiro et al. (2008)), all in good agreement with experiments.

For two successive two-dimensional steep hills, the flow conditions on the second hill are still harder to predict, even for shallow hills. Previous studies like Bitsuamlak et al. (2006), by comparing their numerical simulations with

the experimental data of Carpenter and Locke (1999), have shown that RANS equations predict well the mean velocity field. In the case of sinusoidal smooth hills,Lee et al. (2002) also use both RANS numerical simulations and experiments to analyze the impact of the first hill flow separation on the surface pressure of the second hill. They observe that even at a distance $\lambda = 5H$ between the hills crest, the surface pressure at the second hill crest is about $25 - 30\%$ smaller than at the first hill crest. The difference of surface pressure then decreases as λ increases. Kim et al. (1997) also investigated experimentally the two hill configuration by varying the height of the first hill to observe the impact on the flow over the second hill. For a first hill of height $H_1 = 2H_2$ (where H_2 is the height of the second hill) and a slope of $S = 0.5$, the size of the separation flow area behind the second hill is decreased by 20% from that of the same isolated hill.

Several experimental studies have been conducted to study the separation flow behind the first hill and its disturbance of the flow over the second hill. Li et al. (2017) use a PIV system in a wind tunnel to investigate the velocity and the turbulence intensity around two-dimensional successive smooth hills for installation of wind turbines. For a slope of $S = 0.5$, the measurements show an important production of the turbulent energy in the separation flow area of the first hill. Ferreira et al. (1991) present an experimental investigation of interaction between two 2D smooth hills by varying the distance λ. For a slope $S = 0.5$, Ferreira et al. (1991) observe an increase of maximum velocity at the top of the second hill as the distance λ increases. The size of the separation flow area of the first hill tends to grow as both hills approach each other.

In this study, we present a parametric investigation of rough two-hills flow configurations using a RANS $k - \epsilon$ model and experiments. The experimental set-up and numerical method are presented in section 2. The flow structure and the comparison between the experiments and the numerical simulations are presented and discussed in section 3. Results of the parametric investigation performed with numerical simulations are presented and discussed in section 4. In section 5, the ability of a simple plane mixing layer model to explain

and predict flow caracteristics in the vicinity of the second hill is investigated. Conclusion and perspectives are drawn in section 6.

2. Configuration and method

2.1. Experimental set up

A sketch of the experimental set-up is shown in Figure 1(a). The experiments were performed at the Institut de Mécanique des Fluides de Toulouse (IMFT) in a 26 m long, 1.10 m wide and 0.50 m deep open-channel flume made out of glass with a slope of 0.3 % (see Rouzes et al. (2019) for more detail). In the entry section, the flow passes through a honeycomb and a series of mesh grids before converging at the main channel entry to help establish inlet flow homogeneity and a low background turbulence intensity. The bottom of the flume was covered with an artificial grass of 5 mm height. All experiments were performed with a flow rate of $0.14\ m^3 s^{-1}$. The Reynolds number in the flume, $Re = U_{flow} H_{flow,m}/\nu$, was equal to $1.47\ 10^5$, with $H_{flow,m} = 0.4\ m$ the mean flow depth in all experiments, $U_{flow} = 0.36\ ms^{-1}$ the bulk velocity and $\nu = 10^{-6}\ m^2 s^{-1}$ the kinematic vicosity of water. The Froude number $Fr = U_{flow}/\sqrt{gH}$, was equal to 0.18. With this low value of the Froude number, the water surface deformation generated by the presence of the topographic elements was negligible.

The first hill was always located at a distance equal to 10.5 m from the inlet of the flume. The turbulent boundary developed a thickness larger than the height of the hills. The hills in the experiments were built in polystyrene, attached to glass plates then covered with the same artificial grass as on the flume's bottom surface. All hills had a shape $z_H(x)$ given by :

$$z_H(x) = H \cos^2\left(\frac{\pi x}{2L_u}\right) \tag{1}$$

with H the height of the hill and L_u its width. With this cos^2 shape, the mid-height width L of the hill is equal to L_u, and its slope S is given by $S = H/L = H/L_u$.

This shape was already used in the previous works of Gong and Ibbetson (1989) and Cao et al. (2012). The height and width are sometimes noted with an index i indicating if it concerns the first hill ($i = 1$) or the second one ($i = 2$). Most of the experiments were performed with the same hill's height $H_1 = H_2 = 0.06\ m$ and the same width $L_{u1} = L_{u2} = 0.15\ m$. With these values, the hills can be considered as steep, since their slope is equal to 0.4. They exhibit a clear recirculation downstream as observed by Finnigan (1988).

The flow velocity measurements were performed using a PIV 2D-2C technique. A double cavity pulse laser Nd-Yag (Quantel CFR 2000) with a power of 0.2 J illuminates the flow seeded with glass particles. A CCD camera (PCO 2000) with a resolution of 2048x2048 pix^2 recorded the movement of illuminated particles in the form of a successive pairs of pictures. The PIV plane is placed in the center plane of the flume and it is moved in the streamwise direction to capture the entire flow velocity around the two hills. The camera field of view was 0.415 m x 0.415 m. For all configurations, the acquisition frequency was $F = 4\ s^{-1}$ and 3000 bursts were then recorded in each PIV measurement plane. With this low frequency acquisition, mean flow and second-order statistics in the x and z directions are then inferred from these time-series of uncorrelated instantaneous velocity measurements.

First, an experiment without the hills was carried out to determine the friction velocity u_* and the roughness length z_0 in the turbulent boundary layer at the location of the hills, for reference. Fig 2 shows the vertical profile of the mean longitudinal velocity $\overline{u}$ for this experiment without hills, along with the fitted logarithmic law :

$$\overline{u}(z) = \frac{u_*}{\kappa} ln\left(\frac{z-d}{z_0}\right) \tag{2}$$

where κ is the Von Karman constant, fixed here as $\kappa = 0.41$, u_* is the friction velocity, d is the displacement height and z_0 is the roughness length.

With the experimental data, a friction velocity of $u_* = 0.0239\ ms^{-1}$ is found by extrapolating the vertical profile of the turbulent shear stress $-\overline{u'w'}$ towards $z = d$ (see Florens et al. (2013) and Rouzes et al. (2019)). Values of

$z_0 = 0.49\ 10^{-3}\ m$ and $d = 5.4\ 10^{-3}\ m$ were obtained by fitting the log-law. The value found for the displacement height d indicates that the artificial grass has a very low porosity, with a theoretical plane for the log-law (where the velocity drops to zero) very close to the top of the artificial grass.

The 2D-2C PIV measurement system gives only two components ($\overline{u}$ and $\overline{w}$) of the velocity. For comparison with the numerical simulations, we need to estimate the turbulent kinetic energy $k = \left(\overline{u'^2} + \overline{v'^2} + \overline{w'^2}\right)/2$ in the experiments, with an unmeasured turbulent component $\overline{v'^2}$. In the present study, we will use the same estimate as Nezu and Nakagawa (1993), who proposed the following estimate for the turbulent kinetic energy with experimental data only in the x and z directions, noted k_{exp}, and defined as :

$$k_{exp} = \frac{1}{1.44}\left(\overline{u'^2} + \overline{w'^2}\right) \tag{3}$$

The geometric scaling factor between the experiment and the real atmosphere, noted γ, is equal to $\gamma = 3000$, assuming a typical neutral atmospheric boundary layer of depth $\delta_{real} = 1200\ m$. The experiments are then relevant for hills of real height $H_{real} = 180\ m$ over a land with a roughness length $z_{0,real} = 1.47\ m$ corresponding to dense forests.

2.2. Numerical method

The code Saturne is used to model the flow in the flume around the 2D hills. This code is based on a finite volume approach which solves the following Reynolds Averaged Navier-Stokes equations :

$$\rho\overline{u_j}\frac{\partial\overline{u_i}}{\partial x_j} = -\frac{\partial\overline{p}}{\partial x_i} + \frac{\partial}{\partial x_j}\left(\mu\left(\frac{\partial\overline{u_i}}{\partial x_j} + \frac{\partial\overline{u_j}}{\partial x_i}\right) + R_{ij}\right) \tag{4}$$

$$\frac{\partial\overline{u_j}}{\partial x_j} = 0 \tag{5}$$

with ρ the density, $\overline{u_{i,j}}$ the components of the mean velocity with $i, j = 1\ and\ 3$, $\overline{p}$ the mean pressure and the Reynolds stress tensor $R_{ij} = -\rho\overline{u_i' u_j'}$.

The standard k-ϵ turbulence model is used, reading :

$$\frac{\partial}{\partial t}(\rho k) + \frac{\partial}{\partial x_i}(\rho k \overline{u_i}) = \frac{\partial}{\partial x_j}\left[\left(\mu + \frac{\mu_t}{\sigma_k}\right)\frac{\partial k}{\partial x_j}\right] + \mathcal{P} - \rho\epsilon \tag{6}$$

$$\frac{\partial}{\partial t}(\rho \epsilon) + \frac{\partial}{\partial x_i}(\rho \epsilon \overline{u_i}) = \frac{\partial}{\partial x_j}\left[\left(\mu + \frac{\mu_t}{\sigma_\epsilon}\right)\frac{\partial \epsilon}{\partial x_j}\right] + C_{\epsilon 1}\frac{\epsilon}{k}\mathcal{P} - \rho C_{\epsilon 2}\frac{\epsilon^2}{k} \tag{7}$$

with the turbulent eddy viscosity defined as $\mu_t = \rho C_\mu \dfrac{k^2}{\epsilon}$. C_μ, $C_{\epsilon 1}$, $C_{\epsilon 2}$, σ_k, σ_ϵ are the turbulence model's constants, with values for the classical turbulence model given in table 1). $\mathcal{P}$ is the turbulent kinetic energy production term, given by:

$$\mathcal{P} = -\rho R_{ij}\frac{\partial \overline{u_i}}{\partial x_j} \tag{8}$$

$$= \left[\mu_t\left(\frac{\partial \overline{u_i}}{\partial x_j} + \frac{\partial \overline{u_j}}{\partial x_i}\right) - \frac{2}{3}\rho\, k\, \delta_{ij}\right]\frac{\partial \overline{u_i}}{\partial x_j} \tag{9}$$

For the simulations, a computation domain focused on the region around the two hills was selected to accelerate calculations. A sketch of this computation domain is plotted in Figure 1(b). The inlet boundary is located just before the first hill, at its foot, i.e. $x = -L_u$. The total length of the domain, L_D, extends 84 hill heights, $L_D = 84H_1$ in order to capture the recirculation regions and wakes of both hills. The height of the domain H_{flow} varies along x to follow the small variation of water depth along the flume expected for a non uniform free surface flow.

A non-orthogonal grid is used to mesh the computation domain. A high density mesh is selected in the lower part of the domain (figure 3), close to the hills, in an area corresponding to twice the size of the middle layer defined by

C_μ	$C_{\epsilon 1}$	$C_{\epsilon 2}$	σ_k	σ_ϵ
0.09	1.44	1.92	1	1.3

Table 1: Constants of the standard turbulence model k-ϵ

Hunt et al. (1988). It is in this middle layer, of height $h_m = 0.033\ m$, that most of the perturbation induced by the hills on the velocity and turbulence fields is observed. The size of this lower part was fixed by a convergence study with the vertical size of the cell $\Delta z = 0.017H$, with $H = 0.06\ m$ the height of the hill. In the upper part of the domain we use a geometric progression $\Delta z_{i+1} = q * \Delta z_i$ with the ratio $q = 1.02$ and Δz_1 equal to the Δz in the high density mesh part.

To prescribe the inlet boundary condition, both experimental and numerical data were used. A preliminary numerical simulation was carried out on a larger computation domain, beginning at the entry of the flume, in order to calculate the turbulent boundary layer development. The mean longitudinal profile obtained in this numerical simulation yield a boundary layer thickness smaller than in the experiments at the same location, 10.5 m from the entry.

Since the flow dynamics around the hills is mainly controlled by the incident mean velocity profile, we adopted a hybrid approach for the numerical simulations on the computation domain focused on the hills : for the inlet mean longitudinal velocity $\overline{u}$, we used the experimental data, and for k and ϵ, we used the numerical data of the turbulent boundary layer development simulation. Since $k - \epsilon$ models tend to oversestimate k, it was not possible to choose the experimental estimates of the kinetic energy k_{exp} for the numerical simulation. Moreover, the experiments do not provide any estimates of ϵ, and the vertical profiles of k and ϵ predicted by the turbulent boundary layer development are already in equilibrium. It was not possible to use a logarithm profile for the mean velocity profile since the upstream boundary condition for our simulations is fixed at the entrance of the hill, where the mean flow pattern is already modified by the presence of the hill. In most studies, the inlet boundary condition is chosen at a distance of $5H$ (Franke et al. (2004),Franke and Baklanov (2007)) upstream the hill, where a log-law profile is then prescibed. For the single hill flow configuration, we performed this additional numerical simulation with an inlet boundary located at a distance $5H$ upstream the hill, and inlet flow conditions based upon the log-law profile with the roughness length z_0 found in the experiments without the hill. We then compared the results with those from

our hybrid simulation with an inlet boundary located at the entrance of the hill where experimental measurements of the mean velocity are used instead of a log-law profile. The flow development along the hill, both for the mean flow components, k and ϵ, was exactly the same, showing that our approach is equivalent to the more classical one where a log-law profile is imposed as inlet flow conditions $5H$ upstream the hill.

The lower boundary condition was prescribed using a two scales wall function taking into account both the shear effect and the turbulence effects on the floor. Two friction velocities are considered by the wall function, noted u_k and u_*, calculated at the first node I as :

$$u_k = C_\mu^{1/4} k_I^{1/2} \tag{10}$$

$$u_* = \frac{\overline{u_I}}{\frac{1}{\kappa} ln\left(\frac{z_I + z_0}{z_0}\right)} \tag{11}$$

with a roughness length z_0 in the definition of u_* that is chosen equal to the value measured in the experiments, i.e. $z_0 = 0.49\ mm$. z_I is the distance between the node I and the virtual plane where the log-law velocity drops to 0.

It is assumed that the first node I is located in the log-law region, and boundary conditions for the turbulence quantities k and ϵ are then prescribed at the wall position as :

$$k_{wall} = \frac{u_k^2}{c_\mu^{1/2}} \tag{12}$$

$$\epsilon_{wall} = \epsilon_I + z_I \frac{u_k^3}{\kappa(\frac{z_I}{2} + z_0)^2} \tag{13}$$

For the top and the lateral boundaries of the domain, a rigid lid approximation is applied. In the experiment, the Froude number was so low (around 0.18) that the different topographies did not generate any water surface deformation, allowing such a rigid lid approximation for the numerical model. The normal mean velocity, the tangential velocity gradient, the kinetic turbulent energy k and the turbulent dissipation rate ϵ are all taken as equal to zero.

On the downstream boundary, zero longitudinal gradients are assumed for all variables.

3. Flow around the hills

3.1. Flow structure

Table 2 summarizes the parameters of the experiments and the numerical simulations. Three configurations were investigated with numerical simulations only ($\lambda/H_1 = 5.8$, 8.5 and 19.2).

Time-averaged longitudinal velocity fields $\overline{u}(x, z)$ are plotted in Figure 4 for the experiments and the numerical simulations. At the crest of the hills, close to the wall, by comparison of the upstream mean velocity profile, an increase of 340% of the mean velocity creates a pressure gradient between the upstream face and the downstream face of the hills. This pressure gradient causes a flow separation , with negative velocities found on the downstream face of the hills. The streamlines joining the separation and reattachment points were calculated and plotted in Figure 4. They separate the free flow and the recirculation cell formed behind the first hill. In the range $\lambda/H_1 \in [4.6, 9.2]$, the second hill penetrates the recirculation cell formed in the wake of the first hill, and the reattachment point is located on the second hill. For $\lambda/H_1 > 9.2$, reattachment of the flow occurs upstream the second hill.

Turbulent kinetic energy fields $k(x, z)$ are plotted in Figure 5.The flow separation and recirculation cell formation observed in Figure 4 generates an important free shear flow far away from the solid boundary. The quasi-equilibrium found between turbulence production and dissipation in the incident turbulent boundary layer is broken, and the turbulence production leads to a growing turbulent kinetic energy wake in the wake of the first hill. In the range $\lambda/H_1 \in [4.6, 9.2]$, the second hill is directly struck by this wake of high turbulence energy. For larger separation distances, the turbulent kinetic energy field $k(x, z)$ around the second hill is more similar to the field around an isolated hill, with a local increase of k (close to the wall, increase of 85% for $\lambda/H_1 = 12.9$

and increase of 88% for $\lambda/H_1 = 19.2$) on the upstream face where the local flow acceleration increases the velocity shear and the turbulence production above its near-equilibrium value in the incident turbulent layer.

3.2. Validation of numerical simulations

For comparison, vertical profiles of the mean longitudinal velocity $\overline{u}$ at different positions along the two hills have been plotted in Figure 6 for a dimensionless distance between the hills $\lambda/H_1 = 4.6$. This particular value of λ/H_1 was chosen to have the second hill highly impacted by the wake of the first hill. However, comments and conclusions drawn here have been checked for all available data. For the mean flow component plotted in Figure 6, there is clearly a good agreement between the experiments and the numerical simulations.

Vertical profiles of the turbulent kinetic energy k at different positions along the two hills have been plotted in Figure 7 for the same dimensionless distance between the hills $\lambda/H_1 = 4.6$. With the experimental data, values of k were only estimated using equation (3).

At the entrance of the first hill, Figure 7(a) shows an overestimation of k by the numerical model on the upstream face ($x/H_1 \in [-2, 0]$). This overestimation is a general tendancy observed for any $k - \epsilon$ model describing a developing boundary layer. More interesting, on the downstream face of the first hill, at $x/H_1 = 1.4$, there is a very good accordance between the experiments and the numerical simulation for the peak intensity and spreading of turbulent kinetic energy generated in the wake of the crest of the hill. The main difference there is that the numerical profile exhibits a larger upward diffusion of the turbulent kinetic energy produced in the free velocity shear. At $x/H_1 = 2$, the enhanced diffusion of the turbulent kinetic energy by the numerical model leads to a slight underestimation of 15% of the maximum of k in comparison with the experiment.

In Figures 6 and 7, results of a numerical simulation without hills have been plotted with dashed blue lines for reference. The vertical profiles of the mean longitudinal velocity and the turbulent kinetic energy do not exhibit any strong

modification along the simulation domain, as expected for a turbulent boundary layer in quasi-equilibrium developing slowly along the longitudinal direction. It confirms the homogeneity of the velocity and turbulent kinetic energy along the domain as required by Longo et al. (2017) and Blocken et al. (2007).

On the second hill, Figure 7(b) shows the same tendencies as for the first hill. On the upstream face, there is an overestimation of the turbulent production in the accelerated region leading to a growth of the maximum of k beyond the experimental trend. In the wake of the second hill, the enhanced diffusion by the numerical model of the turbulent kinetic energy yields values slighty below the experimental ones.

This behavior is observed in other simulations presented in the works of Balogh et al. (2012), where an enhanced diffusion caused by the classical turbulence model $k - \epsilon$ creates an underestimation of the turbulent kinetic energy peak in the wake of the hills.

Maxima of the dimensionless error between the experiments and the numerical simulations have been calculated for the different flow configurations and for the two relevant flow components, the mean longitudinal flow velocity $\overline{u}$ and the turbulent kinetic energy k. Errors on the mean longitudinal flow velocity $e_{\overline{u}}$ were normalized by the bulk flow velocity U_{flow} and the errors on the turbulent kinetic energy e_k were normalized by the local maximum. Values are given in Table 3 and are very low for the velocity, with errors below 10%. The turbulence kinetic energy errors are more important.

In terms of wall function validity, is should be noted that in the experiments a fully rough turbulence regime is generated with $z_0^+ = z_0 u_* / \nu \approx 11$. Here, the flow develops along a rough surface, with a first node always out of the roughness sublayer of the artificial grass, in the log law region (see discussion of the flow structure in Florens et al. (2013)). As long as the flow remains in the rough turbulence regime, the wall function remains valid. Values of z_0^+ along the bed have been calculated and remain always larger than two, except in very small area around the stagnation points.

4. Local flow conditions around the second hill

4.1. Effect of the distance λetween the two hills

In figure 8, profiles along the second hill of the mean velocity $\overline{u}$ at a distance $z_{10} = 3.33\ 10^{-3}\ m$ from the surface have been plotted for the eight configurations investigated numerically, in the range $\lambda/H_1 \in [4.6, \infty[$. The value of the distance z_{10} was chosen in order to correspond to a height of 10 m in the real atmospheric flow, a standard for *in situ* wind caracterisation and prediction by meteorologic models. $\lambda/H_1 = \infty$ corresponds to the reference configuration with an isolated hill. Here, both hills have exactly the same height, $H_1 = H_2$ and the same slope $S_1 = S_2 = 0.4$.

For an isolated hill ($\lambda/H_1 = \infty$), the mean velocity $\overline{u}$ increases along the upstream face of hill towards a maximum located at $x/L_u = -0.097$, just before the crest of the hill (located at $x/L_u = 0$). Then $\overline{u}$ drops to negative values on the downstream face, in the separation cell which forms in the wake of the hill. The same mean flow pattern is found when the hill is not strictly isolated but placed at a large distance in the wake of another hill. There is almost no difference between profiles for $\lambda/H_1 = \infty$ and $\lambda/H_1 = 19.2$ in Figure 8.

When λ/H_1 decreases from 19.2, $\overline{u}$ decreases on the upstream face of the second hill, with a shift of the velocity maximum towards the top of the hill. Negative values are even found for $\lambda/H_1 \leq 8.5$, when the second hill begins to penetrate inside the recirculation cell of the first hill.

In figure 8, profiles along second hill of the turbulent kinetic energy k at a distance $z_{10} = 3.33\ 10^{-3}\ m$ from the surface have been plotted for the eight configurations investigated numerically, in the range $\lambda/H_1 \in [4.6, \infty]$.

For an isolated hill ($\lambda/H_1 = \infty$), an increase of the turbulent kinetic energy from its incident value is observed on the upstream face of the hill, with a jump towards a maximum just after the top of the hill, at $x/L_u = 0.077$. Then k drops to values close to zero on the downstream face of the hill, in the recirculation cell.

For a second hill placed at a large distance ($\lambda/H_1 = 19.2$) in the wake of

the first hill, the shape of the profile of turbulent kinetic energy along the hill is similar to the profile for the isolated hill. A higher level of energy is still found on the upstream face, just before the local maximum near the top of the hill found for an isolated hill. It is the remains of the turbulent wake in the lee of the first hill, which has been damped and integrated back inside the turbulent boundary layer. Even for ($\lambda/H_1 = 12.9$), this higher level of energy does not exceed the maximum bump.

However, as the distance between the two hills still decreases below ($\lambda/H_1 < 12.9$), the profile of turbulent kinetic energy k on the usptream face exhibits a bell shape with values far larger than the energy maximum found for the isolated hill. This bell shape coincides with the turbulence patch observed in the wake of the first hill in Figure 5, generated by flow separation on the first hill. This turbulence patch impacts directly the second hill upstream face for $\lambda/H_1 \in [4.6, 9.2]$.

4.2. Effect of slope and height ratios between the two hills

The flow dependence with the distance between the two hills was analyzed for two identical hills in the previous subsection from numerical results. Here, the distance λ is kept constant, equal to $\lambda/H_2 = 8.5$. The second hill has a slope and and height kept constant in the three configurations, with $S_2 = 0.4$ and $H_2 = 0.06\ m$ like in the previous subsection. For the first hill, three different values of slopes and heights are investigated. $S_1 = 0.4$ with $H_1 = H_2 = 0.06\ m$ is the reference case whereas $S_1 = 0.4$ with $H_1 = 2H_2 = 0.12\ m$ and $S_1 = 0.8$ with $H_1 = 2H_2 = 0.12\ m$ are considered. We have three numerical configurations that we investigate to study effect of slope and height ratios between the two hills.

Time-averaged longitudinal velocity and turbulent kinetic energy fields $\overline{u}(x, z)$ and $k(x, z)$ are plotted in Figure 10 for the three configurations. In the time-averaged longitudinal velocity field, the shape of the recirculation cell in the wake of the first hill appears to scale with the height of the hill. However, for the same value of H_1, for which a similar recirculation cell is observed, the

level of kinetic turbulent energy k is higher for the hill with the highest slope $S_1 = 0.8$. In figure 10(b) for this configuration with $S_1 = 0.8$, the flow acceleration on the upstream face of the first hill already generates higher levels of turbulent kinetic energy than for $S_1 = 0.4$. This initial increase leads to a higher level of turbulent kinetic energy impacting the second hill.

In figures 11 and 12, profiles along the second hill of the mean velocity $\overline{u}$ and the turbulent kinetic energy k at a distance $z_{10} = 3.33\ 10^{-3}\ m$ from the surface have been plotted for the three configurations. For the two configurations where the first hill is higher than the second hill, i.e. $H_1 = 2H_2$, the second hill is completely embedded in the recirculation cell, with mainly negative values of the tangential velocity when the first hill has the same slope as the second hill ($S_1 = 0.4$) and negative everywhere when the first hill has a steeper slope ($S_1 = 0.8$). This small difference indicates a slighty deeper recirculation cell behind the first hill with the steepest slope. In the profiles of the turbulent kinetic energy k in Figure 12, a higher level of turbulent kinetic energy is clearly found in the wake of the steepest hill. It indicates that the flow over the second hill depends also on turbulent kinetic energy generated on the upstream slope of the first hill by flow acceleration and velocity gradient increase.

5. Discussion

The recirculation cell in the wake of the first hill disturbs the flow around the second hill both in terms of velocity and turbulent kinetic energy when the second hill is close to this flow region. From the detachment point near the top of the first hill along the streamine plotted in Figures 4 and 5, the flow is very similar to a planar mixing layer growing along the velocity discontinuity formed between the flow above and the recirculation cell. The planar mixing layer can be modeled by a simple turbulence model (see Pope (2000)) to describe its development along a velocity discontinuity between two flow regions of parallel velocities U_t and U_b. From U_t and U_b, two new velocities are introduced, the

convective velocity U_c and the velocity difference U_s defined as :

$$U_c = \frac{1}{2}\left(U_t + U_b\right) \tag{14}$$

$$U_s = U_t - U_b \tag{15}$$

Here, to apply this simple model to the mixing layer developing along the detached streamline behind the first hill, we estimate that the relevant values for U_t and U_b are, respectively, the value of the velocity near the detachment point at $\Delta z = z - z_{hill} = 0.2H_1$, and 0. The choice of 0 as a value for U_b results from the fact that near the detachment point, the velocity below the separation streamline is close to zero. Of course, as the mixing layer develops longitudinally and entrains the fluid below, a recirculation cell forms. Yet, the weak negative counter-flow found in the lower part of the cell should not be taken into account for the estimation of U_b.

For self-similarity analysis, scaled coordinates ζ and velocity F are introduced and defined as :

$$\zeta = \frac{z - z_c(x)}{\delta(x)} \tag{16}$$

$$F(\zeta) = \frac{U(z) - U_c}{U_s} \tag{17}$$

where $z_c(x)$ is the vertical coordinate of the center of the mixing layer and $\delta(x)$ is the thickness of the mixing layer.

The mixing layer thickness is defined as $\delta(x) = z_{0.9}(x) - z_{0.1}(x)$, where $z_{0.9}(x)$ and $z_{0.1}(x)$ are the altitude where $\overline{u}(z) - U_c = 0.4U_s$ and $\overline{u}(z) - U_c = -0.4U_s$, respectively.

The center $z_c(x)$ of the mixing layer may be defined with the detached streamline as $z_c(x) = z_s(x)$, with $z_s(x)$ the coordinate of this streamline, or as $z_c(x) = z_m(x)$, with $z_m = 0.5(z_{0.9}(x) + z_{0.1}(x))$, as in Pope (2000).

In Figure 13, profiles of the scaled velocity F are plotted at different positions in the wake of the first hill with the two definitions of z_c. The reattachment point is located at $x/H_1 = 6.7$ for this flow configuration. Both definitions of

z_c lead to self-similar profiles. Yet, with definition $z_c = z_m$ in Figure 13(b), the level of self-similarity is higher than with definition $z_c = z_s$.

Bell and Mehta (1990) fitted a mixing layer velocity profile with an error function reading

$$F(\zeta) = \frac{erf(\zeta) + a}{b} \tag{18}$$

where a and b are fitting parameters.

When applied to our data, this fitting function gives good results with $a = -0.46$ and $b = 1.65$ for $z_c = z_s$ and $a = 0$ and $b = 1.4$ for $z_c = z_m$. By extrapolating this fitting formula to the location on the upstream face of the second hill, we can then estimate the velocity distribution there expected from the development of the mixing layer.

In Figure 14, profiles of the scaled turbulent kinetic energy k/U_s^2 have been plotted. With the definition $z_c = z_s$, profiles of Figure 14(a) show that the scaled turbulent kinetic energy profiles have an almost constant maximum. However, a gradual drift of this maximum is observed towards $\zeta = 0.6$ for $x/H_1 = 6.7$, the reattachment position of the separation flow behind the first hill. It indicates a drift of the turbulent kinetic energy upwards from the detachment streamline. It is in disagreement with what is observed in pure planar mixing layers. With the definition $z_c = z_m$, profiles of Figure 14(b) are self-similar, without the shift observed with the other definition for z_c. In the lower part of the mixing layer ($\zeta \in [-0.4, -1]$), a lower level of self similarity is observed as the mixing layer develops, due to the presence of the solid boundary below.

For flow configurations with $\lambda/H_1 \in [12.9, 19.2]$, the reattachement point of the detached streamline is located on the bed, upstream the second hill. In that case, we cannot expect self-similarity to hold since the mixing layer will impact first the bed and grow as a boundary layer before arriving on the second hill. To illustrate this loss of self-similary, profiles of the scaled turbulent kinetic energy $k(\zeta)/U_s^2$ in the wake of the first hill have been plotted in Figure 15 for flow configuration $\lambda/H_1 = 12.9$. Self-similarity is gradually lost in the lower part of the mixing layer, as its thickness increases and interaction with the bottom

boundary increases.

In Figure 16, profiles of the mixing layer thickness $\delta(x)$ along the longitudinal direction have been plotted for all available flow configurations. The growth of δ is independant of λ/H_1 parameter and is in good agreement with the linear law proposed by Dimotakis (1991), reading $\delta(x) = D(U_s/U_c)x$, with a fitting parameter $D = 0.1$.

When extrapolated at the position of the second hill, self-similar profiles of the turbulent kinetic energy for the mixing layer generates the bell shape on the upstream face of the second hill visible in Figure 9 for $\lambda/H_1 \in [5.8, 9.2]$, i.e. when the two hills are close enough for the mixing layer to get reattached on the second hill.

6. Conclusion

For a neutral flow over 2D successive steep hills, the comparison with experiments shows that a standard k-ϵ model gives a good estimation of both the mean velocity field and turbulent kinetic energy, with normalized errors below 10% and 20%, respectively. It gives also conservative estimates of the local flow conditions along the second hill, useful for pylon design. In the present study, this good estimation by a standard k-ϵ model is obtained by using measurements of the vertical profile of mean velocity to prescribe inlet conditions at the entrance of the first hill. It was checked by additional numerical simulations (not shown here) that the use of the logarithmic profile at a larger distance in front of the first hill (typically $5H$) yield the similar results. These additional numerical simulations also showed how the velocity profile at the entrance of the first hill was already modified by the presence of the hill (see Figure 6(a) for $x/H_1 = -2$ to see this impact at the entrance of the first hill).

The decrease of the distance between the hills creates a decrease in the mean velocity $\overline{u}$ on the upstream face of the second hill. The turbulent kinetic energy on the upstream face of the second hill exhibits two trends. For $\lambda/H_1 \in [8.5, +\infty]$, the turbulent energy k increases with the decrease of λ. Then, for

$\lambda/H_1 \in [6.9, 4.6]$, the turbulent kinetic energy is controlled by the impacting mixing layer and its maximum remains at the same level. The increase of slope S of the first hill generates a faster initial growth of the turbulent kinetic energy before detachment, so that the subsequent mixing layer development leads to higher levels of turbulence.

To explain and predict the local flow conditions on the second hill, we compared our flow with an analytical model of planar mixing layer. This approach allows us to propose a very simple explanation and quantitative prediction of the kinetic turbulent energy profile on the second hill when the second hill penetrates inside the recirculation cell of the first hill. To use this predictive model, it is possible to consider a mixing layer developing between a fast flow with a velocity given by the velocity at the top of the first hill and zero for the slow flow. The velocity at the top of the first hill can be estimated with the velocity at $z = H_1$ in the incident boundary layer, or by taking the velocity predicted with the model of Hunt et al. (1988). The proposed model is only valid for a neutral boundary layer, and is therefore most appropriate for strong wind conditions.

References

Balogh, M., Parente, A., Benocci, C., 2012. Rans simulation of abl flow over complex terrains applying an enhanced k- epsilon model and wall function formulation: Implementation and comparison for fluent and openfoam. Journal of Wind Engineering and Industrial Aerodynamics 104-106, 360 – 368. URL: http://www.sciencedirect.com/science/article/pii/S0167610512000475, doi:https://doi.org/10.1016/j.jweia.2012.02.023. 13th International Conference on Wind Engineering.

Bell, J.H., Mehta, R.D., 1990. Development of a two-stream mixing layer from tripped and untripped boundary layers. AIAA journal 28, 2034–2042.

Bitsuamlak, G., Stathopoulos, T., Bdard, C., 2006. Effects of upstream two-

dimensional hills on design wind loads: A computational approach. Wind and Structures 9. doi:10.12989/was.2006.9.1.037.

Blocken, B., Stathopoulos, T., Carmeliet, J., 2007. Cfd simulation of the atmospheric boundary layer: wall function problems. Atmospheric Environment 41, 238 – 252. URL: http://www.sciencedirect.com/science/article/pii/S135223100600834X, doi:https://doi.org/10.1016/j.atmosenv.2006.08.019.

Cao, S., Wang, T., Ge, Y., Tamura, Y., 2012. Numerical study on turbulent boundary layers over two-dimensional hills effects of surface roughness and slope. Journal of Wind Engineering and Industrial Aerodynamics 104106, 342 – 349. URL: http://www.sciencedirect.com/science/article/pii/S0167610512000463, doi:http://dx.doi.org/10.1016/j.jweia.2012.02.022. 13th International Conference on Wind Engineering.

Carpenter, P., Locke, N., 1999. Investigation of wind speeds over multiple two-dimensional hills. Journal of Wind Engineering and Industrial Aerodynamics 83, 109 – 120. URL: http://www.sciencedirect.com/science/article/pii/S0167610599000653, doi:http://dx.doi.org/10.1016/S0167-6105(99)00065-3.

Castro, I.P., Apsley, D.D., 1997. Flow and dispersion over topography: A comparison between numerical and laboratory data for two-dimensional flows. Atmospheric Environment 31, 839 – 850. URL: http://www.sciencedirect.com/science/article/pii/S1352231096002488, doi:http://dx.doi.org/10.1016/S1352-2310(96)00248-8.

Dimotakis, P., 1991. Turbulent free shear layer mixing and combustion. High Speed Flight Propulsion Systems 137, 265–340.

Ferreira, A., Silva, M., Viegas, D., Lopes, A., 1991. Wind tunnel simulation of the flow around two-dimensional hills. Journal of Wind Engineering and Industrial Aerodynamics 38, 109 – 122. URL: http://www.sciencedirect.

com/science/article/pii/016761059190033S, doi:https://doi.org/10.1016/0167-6105(91)90033-S.

Finnigan, J., 1988. Air flow over complex terrain, in: Steffen, W., Denmead, O. (Eds.), Flow and Transport in the Natural Environment: Advances and Applications. Springer Berlin Heidelberg, pp. 183–229. URL: http://dx.doi.org/10.1007/978-3-642-73845-6_13, doi:10.1007/978-3-642-73845-6_13.

Finnigan, J., Raupach, M., Bradley, E., Aldis, G., 1990. A wind tunnel study of turbulent flow over a two-dimensional ridge. Boundary-Layer Meteorology 50, 277–317. URL: http://dx.doi.org/10.1007/BF00120527, doi:10.1007/BF00120527.

Florens, E., Eiff, O., Moulin, F., 2013. Defining the roughness sublayer and its turbulence statistics. Experiments in Fluids 54, 1500. URL: https://doi.org/10.1007/s00348-013-1500-z, doi:10.1007/s00348-013-1500-z.

Franke, J., Baklanov, A., 2007. Best practice guideline for the CFD simulation of flows in the urban environment: COST action 732 quality assurance and improvement of microscale meteorological models. Meteorological Inst.

Franke, J., Hirsch, C., Jensen, A., Krs, H., Schatzmann, M., Westbury, P., Miles, S., Wisse, J., Wright, N., 2004. Recommendations on the use of cfd in wind engineering. Proceedings of the International Conference on Urban Wind Engineering and Building Aerodynamics .

Gong, W., Ibbetson, A., 1989. A wind tunnel study of turbulent flow over model hills. Boundary-Layer Meteorology 49, 113–148. URL: http://dx.doi.org/10.1007/BF00116408, doi:10.1007/BF00116408.

Griffiths, A., Middleton, J., 2010. Simulations of separated flow over two-dimensional hills. Journal of Wind Engineering and Industrial Aerodynamics 98, 155 – 160. URL: http://www.sciencedirect.com/science/article/pii/S0167610509001214, doi:https://doi.org/10.1016/j.jweia.2009.10.011.

Hunt, J.C.R., Leibovich, S., Richards, K.J., 1988. Turbulent shear flows over low hills. Quarterly Journal of the Royal Meteorological Society 114, 1435–1470. URL: http://dx.doi.org/10.1002/qj.49711448405, doi:10.1002/qj.49711448405.

Jackson, P.S., Hunt, J.C.R., 1975. Turbulent wind flow over a low hill. Quarterly Journal of the Royal Meteorological Society 101, 929–955. URL: http://dx.doi.org/10.1002/qj.49710143015, doi:10.1002/qj.49710143015.

Kim, H.G., Lee, C.M., Lim, H., Kyong, N., 1997. An experimental and numerical study on the flow over two-dimensional hills. Journal of Wind Engineering and Industrial Aerodynamics 66, 17 – 33. URL: http://www.sciencedirect.com/science/article/pii/S016761059700007X, doi:https://doi.org/10.1016/S0167-6105(97)00007-X.

Lee, S.J., Lim, H., Park, K.C., 2002. Wind flow over sinusoidal hilly obstacles located in a uniform flow. Wind and Structures 5. doi:10.12989/was.2002.5.6.515.

Li, Q., Maeda, T., Kamada, Y., Yamada, K., 2017. Experimental investigation of flow over two-dimensional multiple hill models. Science of The Total Environment 609, 1075 – 1084. URL: http://www.sciencedirect.com/science/article/pii/S0048969717319794, doi:https://doi.org/10.1016/j.scitotenv.2017.07.259.

Longo, R., Ferrarotti, M., Garcia-Sanchez, C., M., D., A., P., 2017. Advanced turbulence models and boundary conditions for flows around different configurations of ground-mounted buildings. Journal of Wind Engineering and Industrial Aerodynamics 167, 160–182. doi:https://doi.org/10.1016/j.jweia.2017.04.015.

Loureiro, J.B., Alho, A.T., Freire, A.P.S., 2008. The numerical computation of near-wall turbulent flow over a steep hill. Journal of Wind

Engineering and Industrial Aerodynamics 96, 540 – 561. URL: http://www.sciencedirect.com/science/article/pii/S0167610508000160, doi:https://doi.org/10.1016/j.jweia.2008.01.011.

Mason, P.J., King, J.C., 1985. Measurements and predictions of flow and turbulence over an isolated hill of moderate slope. Quarterly Journal of the Royal Meteorological Society 111, 617–640. URL: http://dx.doi.org/10.1002/qj.49711146818, doi:10.1002/qj.49711146818.

Mason, P.J., Sykes, R.I., 1979. Flow over an isolated hill of moderate slope. Quarterly Journal of the Royal Meteorological Society 105, 383–395. URL: http://dx.doi.org/10.1002/qj.49710544405, doi:10.1002/qj.49710544405.

Nezu, I., Nakagawa, H., 1993. Turbulence in Open-Channel Flows. A.A. Balkema, Rotterdam.

Pope, S.B., 2000. Turbulent Flows. Cambridge University Press. doi:10.1017/CBO9780511840531.

Rouzes, M., Moulin, F.Y., Florens, E., Eiff, O., 2019. Low relative-submergence effects in a rough-bed open-channel flow. Journal of Hydraulic Research 57, 139–166. URL: https://doi.org/10.1080/00221686.2018.1478894, doi:10.1080/00221686.2018.1478894, arXiv:https://doi.org/10.1080/00221686.2018.1478894.

Safaei Pirooz, A.A., Flay, R.G.J., 2018. Comparison of speed-up over hills derived from wind-tunnel experiments, wind-loading standards, and numerical modelling. Boundary-Layer Meteorology 168, 213–246. URL: https://doi.org/10.1007/s10546-018-0350-x, doi:10.1007/s10546-018-0350-x.

Taylor, P., Teunissen, H., 1987. The askervein hill project: Overview and background data. Boundary-Layer Meteorology 39, 15–39. URL: http://dx.doi.org/10.1007/BF00121863, doi:10.1007/BF00121863.

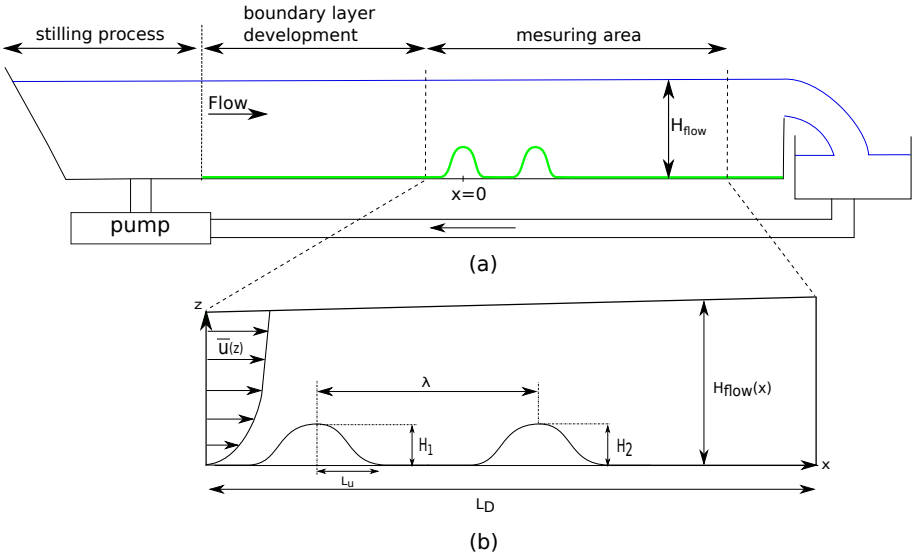

Figure 1: (a) Sketch of the experiment. (b) Sketch of the numerical model

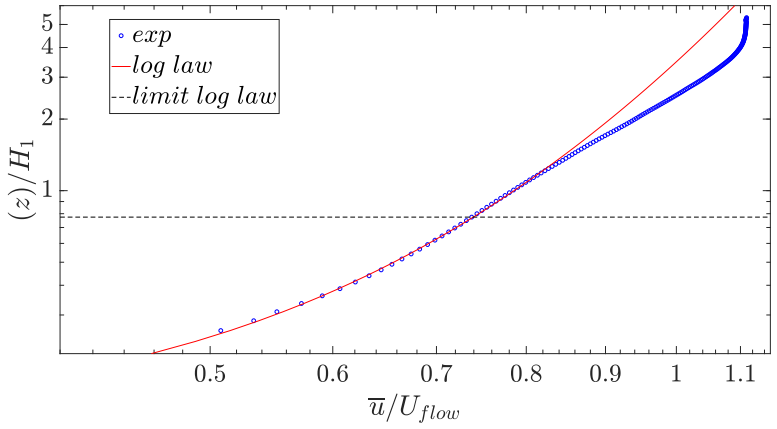

Figure 2: Vertical profile of the mean longitudinal velocity $\overline{u}$ at 10.5 m from the flume's entry in the experiment over the artificial grass without hills. The measurement location corresponds to the location of the first hill in the study. Experimental data are plotted in blue, and the fitted logarithmic law (eq 2) in red. The horizontal dashed line gives the upper bound of the log-law region.

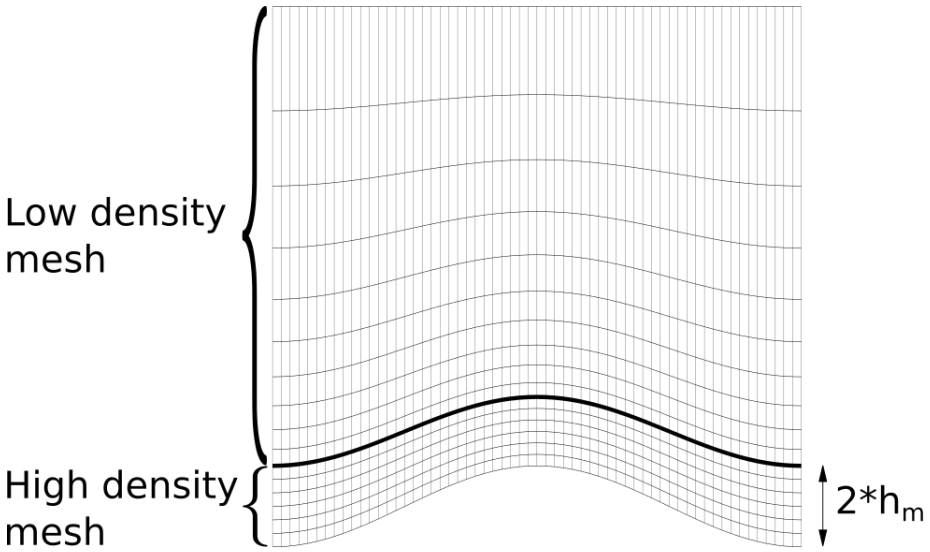

Figure 3: Sketch of the mesh used in the computation domain.

			experiment	simulation
Re_H	H_1/L	z_0(m)	λ/H_1	
2.1 10^4	0.4	0.49 10^{-3}	4.6	4.6
			//	5.8
			6.9	6.9
			//	8.5
			9.2	9.2
			12.9	12.9
			//	19.2

Table 2: Table of numerical and experimental configurations

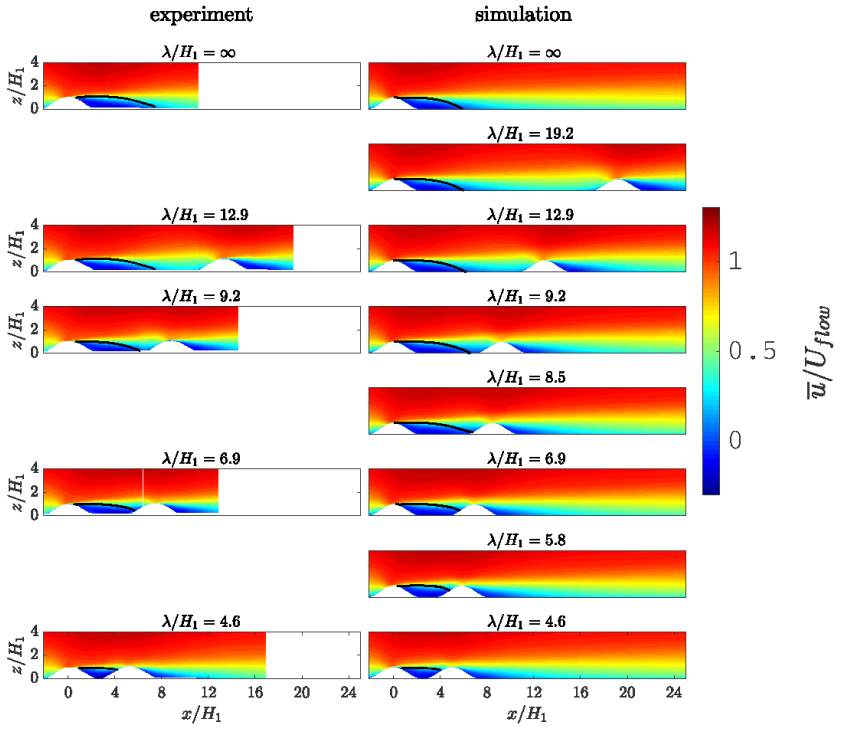

Figure 4: Mean longitudinal velocity fields $\overline{u}(x, z)$ for different values of the dimensionless separation distance λ/H. Experimental and numerical data are plotted, respectively on the left and the right. The black solid line shows the streamline between the separation and reattachment points.

λ/H_1	$e_{\overline{u}}$ (%)	e_k (%)
4.6	6.7	17
6.9	8.3	13.3
9.2	9.1	12.7
12.9	9.3	14.1

Table 3: Maximum of the normalized error between the experiments and the numerical simulations for the mean longitudinal velocity $\overline{u}$ and the turbulent kinetic energy k.

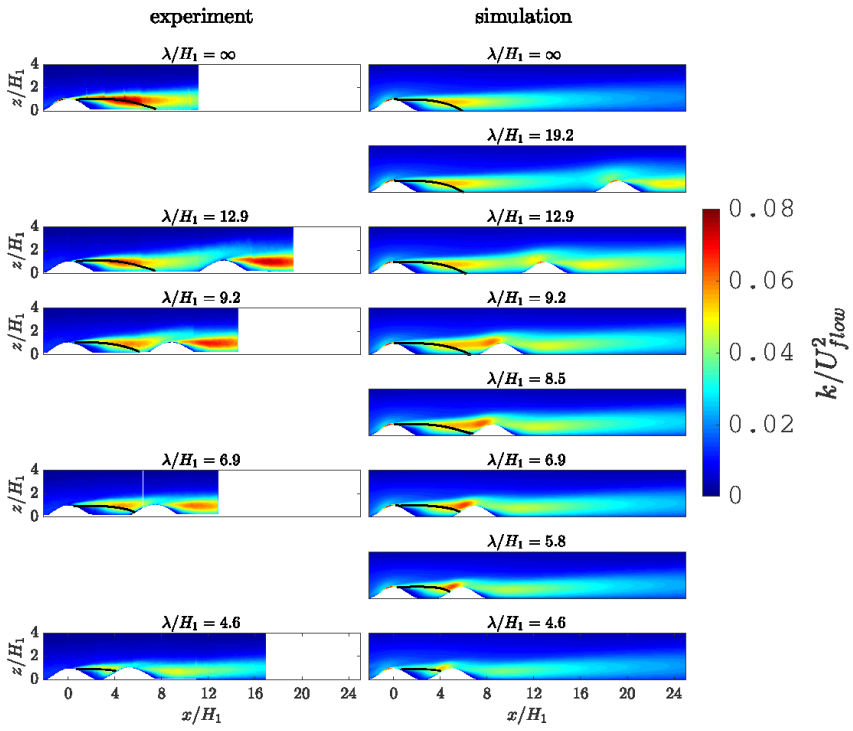

Figure 5: Turbulent kinetic energy fields $k(x, z)$ for different values of the dimensionless separation distance λ/H. Experimental and numerical data are plotted, respectively on the left and the right. The black solid line shows the streamline between the separation and reattachment points.

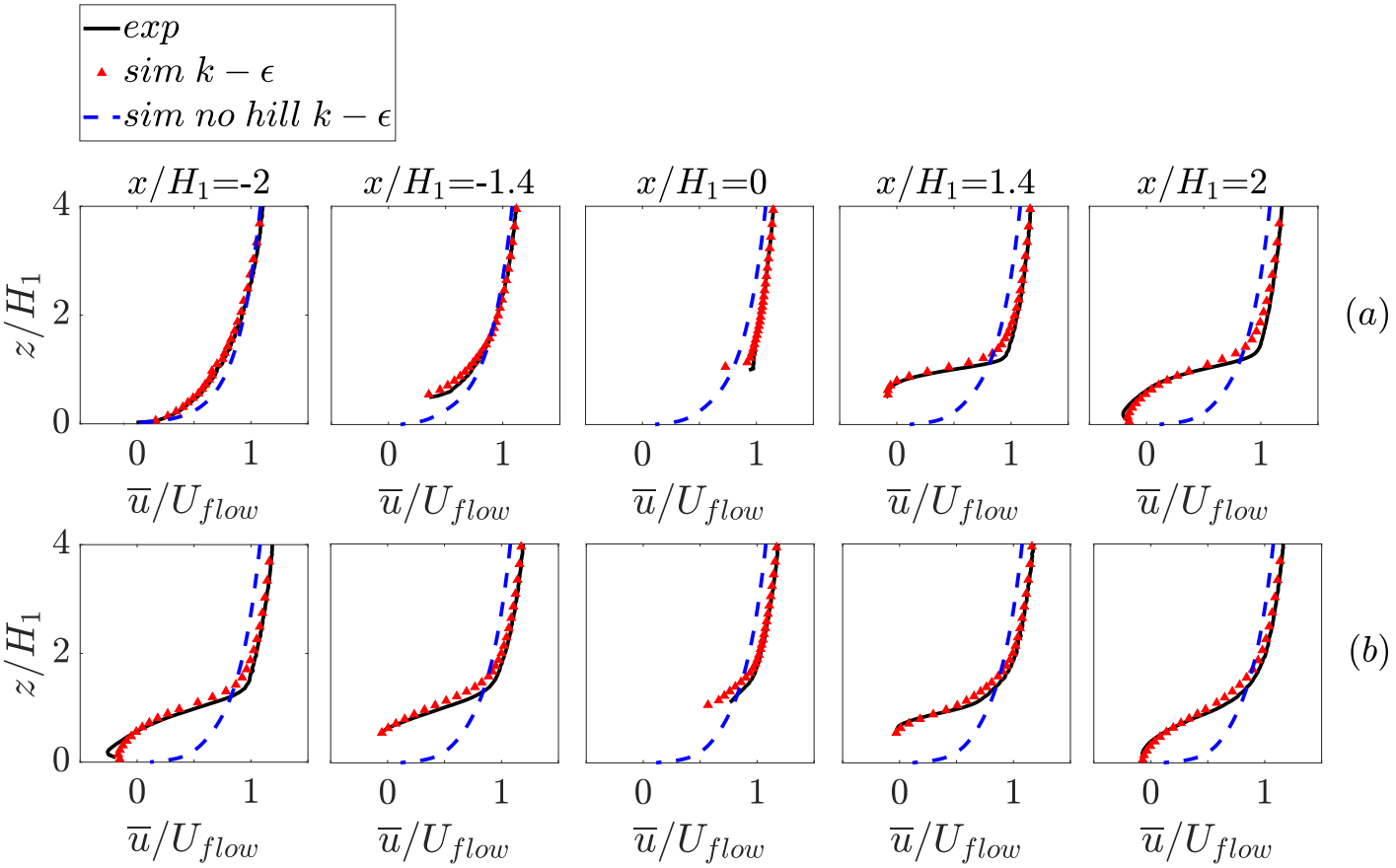

Figure 6: Vertical profiles of the mean longitudinal velocity $\overline{u}$ at different positions x along (a) the first hill and (b) the second hill for a dimensionless distance between the hills $\lambda/H_1 = 4.6$. Black dots are experimental data. Red triangles represent numerical results. Blue dash represent numerical results of configuration without hills.

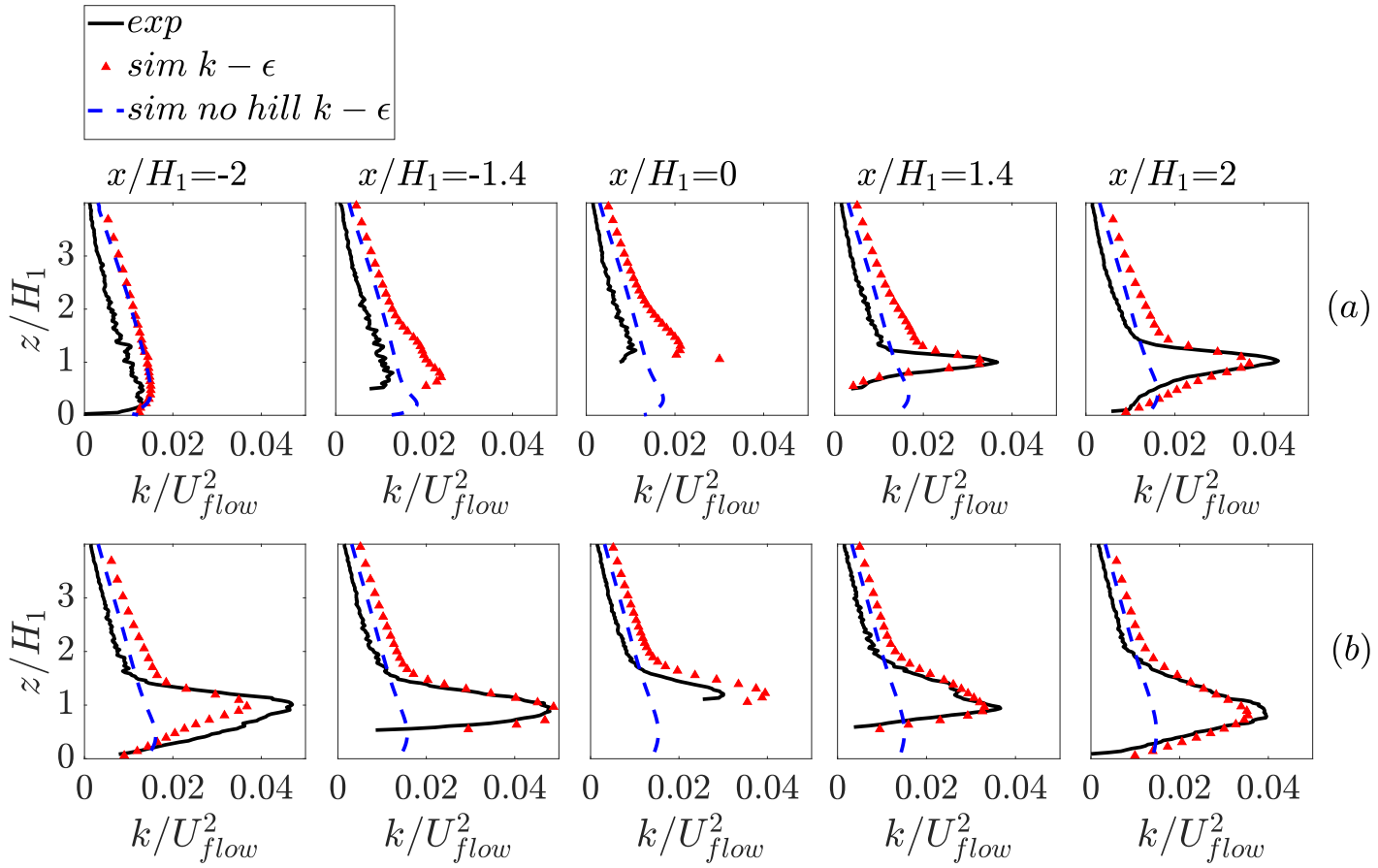

Figure 7: Vertical profiles of the turbulent kinetic energy k at different positions x along (a) the first hill and (b) the second hill for a dimensionless distance between the hills $\lambda/H_1 = 4.6$. Black dots are experimental data. Red triangles represent numerical results. Blue dash represent numerical results of configuration without hills.

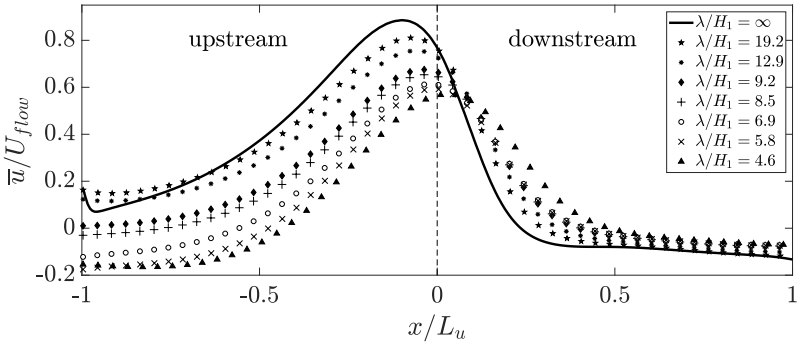

Figure 8: Mean velocity $\overline{u}(z = z_{10} = 3.33\ 10^{-3}\ m)$ over the second hill as function of λ/H_1

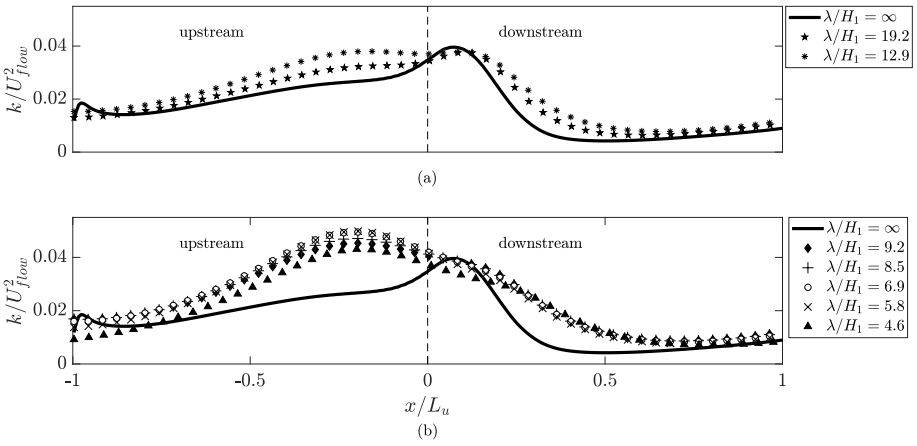

Figure 9: Turbulent kinetic energy $k(z = z_{10} = 3.33\ 10^{-3}\ m)$ over the second hill as function of λ/H_1. (a): for distant hills, (b): for close hills

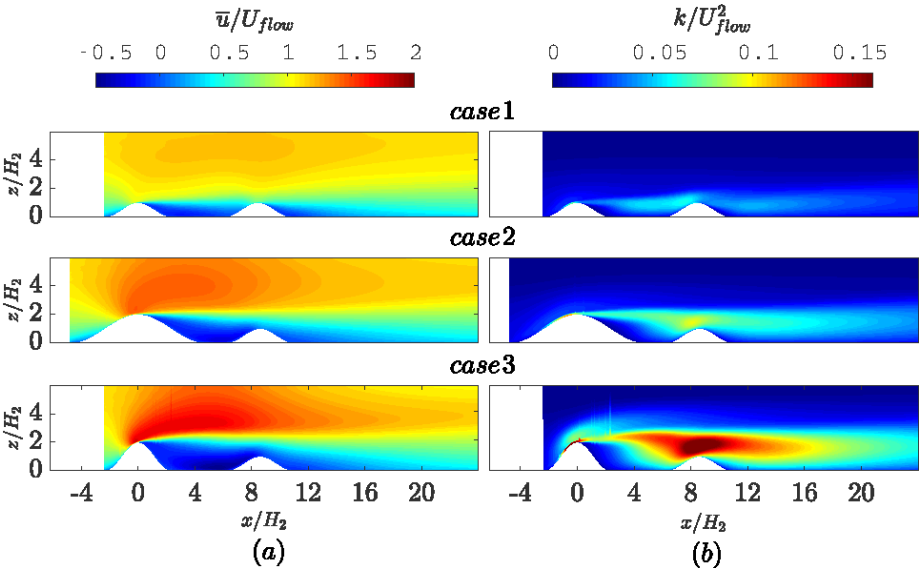

Figure 10: (a) mean longitudinal velocity $\overline{u}(x,z)$ and (b) turbulent kinetic energy $k(x,z)$ fields for a constant dimensionless separation distance $\lambda/H_2 = 4.6$ and different shapes of the first hill. Upper configuration : $H_1 = H_2$ and $S_1 = S_2 = 0.4$. Middle configuration : $H1 = 2H2$ and $S_1 = S_2 = 0.4$. Lower configuration : $H_1 = 2H_2$ and $S_1 = 2S_2 = 0.8$.

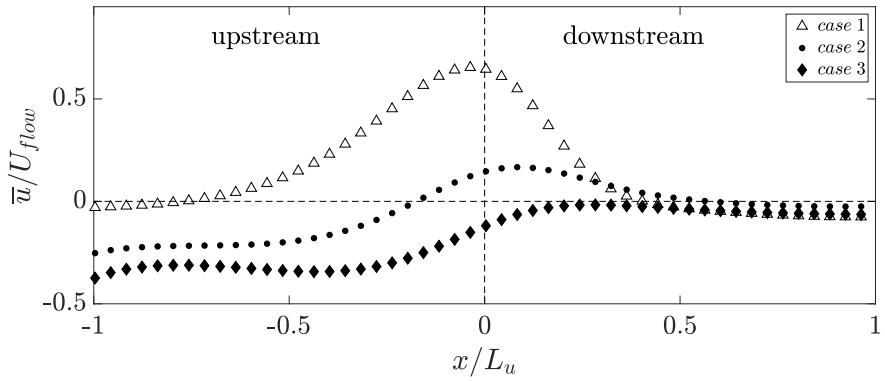

Figure 11: Profiles along the second hill of the mean velocity at a distance $z = z_{10} = 3.33\ 10^{-3}\ m$ from the surface, $\overline{u}(z = z_{10})$ for a constant dimensionless separation distance $\lambda/H_2 = 4.6$ and different shapes of the first hill.

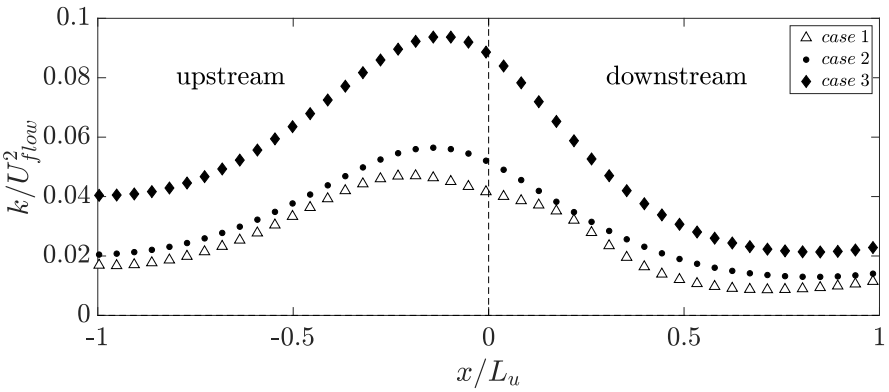

Figure 12: Profiles along the second hill of the turbulent kinetic energy at a distance $z = z_{10} = 3.33\ 10^{-3}\ m$ from the surface, $k(z = z_{10})$ for a constant dimensionless separation distance $\lambda/H_2 = 4.6$ and different shapes of the first hill.

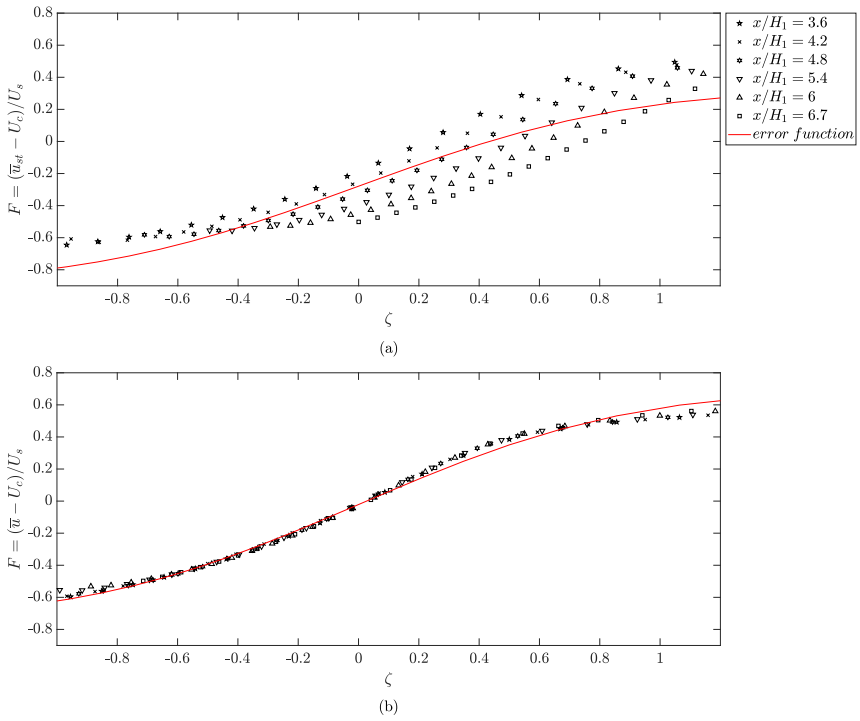

Figure 13: Profiles of the scaled velocity $F(\zeta)$ in the mixing layer at different longitudinal positions in the wake of the first hill, for the flow configuration with $\lambda/H_1 = 8.5$. The scaled coordinate is defined with a center position velocity z_c in the velocity profile defined as (a) $z_c = z_s$ or (b) $z_c = z_m$ (see text for definitions of z_s and z_m).

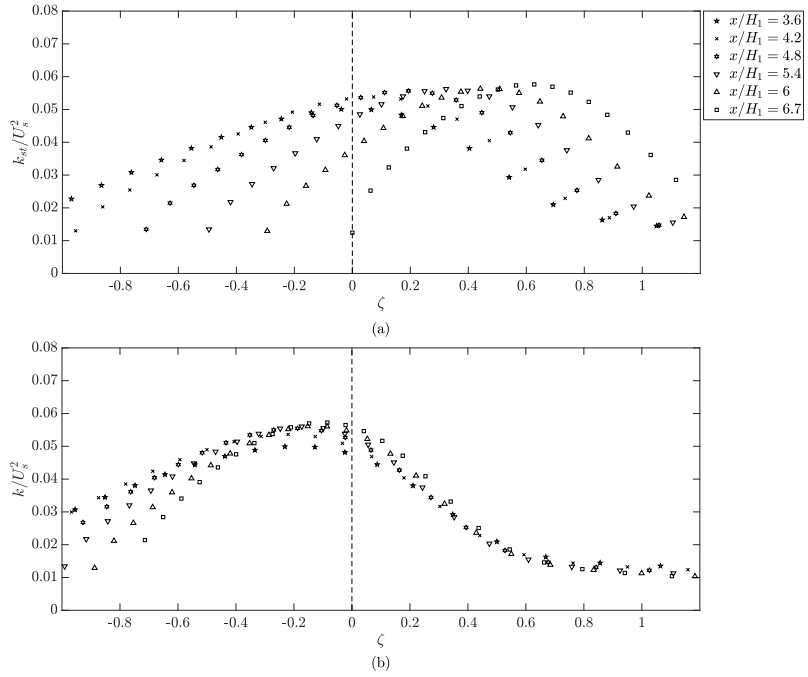

Figure 14: Profiles of the scaled turbulent kinetic energy $k(\zeta)/U_s^2$ in the mixing layer at different longitudinal positions in the wake of the first hill, for the flow configuration with $\lambda/H_1 = 8.5$. The scaled coordinate is defined with a center position velocity z_c in the velocity profile defined as (a) $z_c = z_s$ or (b) $z_c = z_m$ (see text for definitions of z_s and z_m).

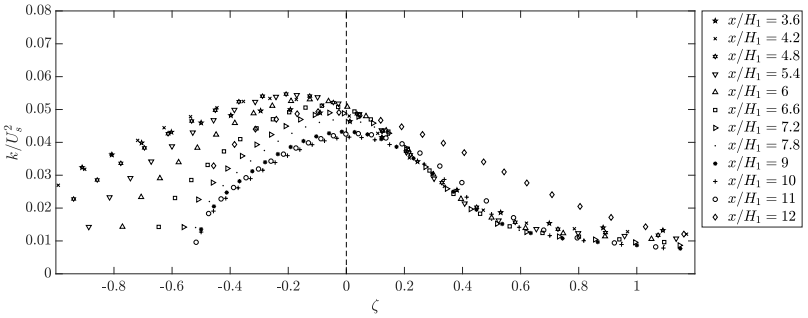

Figure 15: Profiles of the scaled turbulent kinetic energy $k(\zeta)/U_s^2$ in the mixing layer at different longitudinal positions in the wake of the first hill, for the flow configuration with $\lambda/H_1 = 12.9$. The scaled coordinate is defined with a center position velocity z_c defined as $z_c = z_m$).

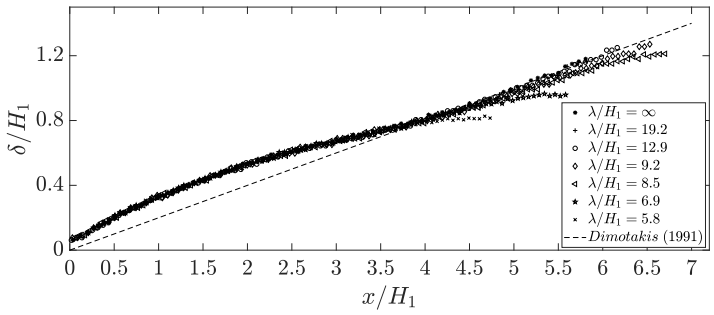

Figure 16: Longitudinal profiles of the mixing layer thickness $\delta(x)$ for different values of λ/H_1. The dashed line is the prediction by Dimotakis (1991) for a planar mixing layer.